

# On Stress Driven Diffusion in Bone - An Experimental Study

Gustav Lindberg<sup>a</sup> and Per Ståhle<sup>b</sup>

<sup>a</sup>*Solid Mechanics, Dept. of Eng. Mech., KTH Royal Institute of Tech. Stockholm, Sweden,*

<sup>b</sup>*Solid Mechanics, Lund Institute of Technology, Lund University, Lund, Sweden,*

---

## Abstract

The transport of nutrients or signal constituents that stimulate growth of bone tissue is supposed to be affected by a static mechanical load. It follows from basic thermodynamical principles that constituents causing volumetric change are dragged along the gradients of hydrostatic stress. The present preliminary study examines the behaviour of iodine present in the medullary cavity of a bovine long bone exposed to mechanical load. A section of the bone is x-ray scanned with the static load present, with and without the iodine. The resulting distribution in a selected 2D plane is numerically evaluated using a discrete Radon's inverse transform. The result suggests that iodine is a useful constituent with a good attenuation effect on the x-ray beam and clearly reveals the temporal distribution of its transport through the bone. It further result shows some indication that stress does affect the iodine distribution. .

*Keywords:* Stress-driven diffusion, tomography, bone, experimental, Radon's integral

---

## 1. Introduction

Bone alters its shape and structure when subjected to mechanical loading [1-3]. The hollow cross-sections of long bones offer a density effective mean for supporting a large variety of loading modes. It has been shown that long bones grow in places where the stress is large to form a cross-section that increases its load carrying capacity and by decreasing the largest cross-sectional stress [4-6].

Low physical activity, e.g., bed rest or being under low-gravity conditions, leads to bone tissue resorption, whereas increased activity stimulates bone growth. Moreover, it has been observed that static loading does not cause bone modelling [7]. From a mechanical perspective the most effective way to strengthen a long bone is to add bone at the outer surface, i.e., the periosteal surface. This increases the elastic section modulus and therefore makes it less prone to fracture.

The present investigation, is motivated by the proposal that the modelling process is governed by changes in the chemical environment at the periosteal

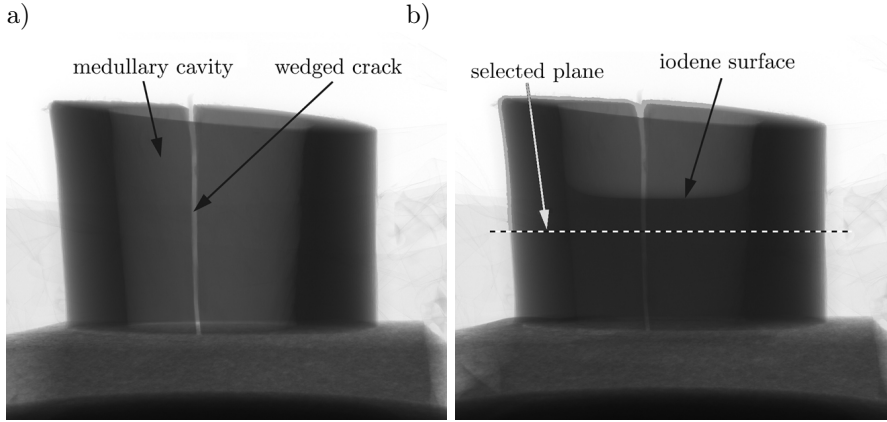


Figure 1: Bone sample a) without iodine, and b) with iodine inserted into the medullary cavity. The iodine volume is the darkened part below the marked iodine surface.

surface. The hypothesis focuses on molecular transport in solids, driven by the gradients of the mechanical stress, as derived by Einstein and observed by Smoluchowski [8, 9]. In the present case the transport from the medullary cavity to the periosteal surface is considered. In the present pilot study iodine is selected as a replacement substance for its large cross-sectional optical area leading to a significant scattering and attenuation of the x-ray beam.

## 2. Samples and experiment

The x-ray scanning was performed at The Henry Moseley X-ray Imaging Facility, Photon Science Institute at the University of Manchester. The scanned sample of an around  $36 \pm 2.5$ mm high bovine long bone with an ellipsoidal cross-section with 39mm and 53mm across. Fig. 1 shows the starting points for two scan series made first without, and then with, an iodine solution introduced into the medullary cavity. The crack that is visible in the figure is opened by a plastic wedge. A silicon adhesive was used for sealing the opened crack to prevent leakage. The same adhesive was used to attach the bone to a polycarbonate plate which was used to support the bone.

Altogether 6284 scans were made at equiangular steps from -180 to 180 degrees for each of the two tests. Each image have a resolution of 4000 times 4000 pixels using 16 bits representing the grayscale. The duration of a full scan was a couple of minutes. The duration between the first test without and the second with the iodine solution was close to 30 minutes.

## 3. Reconstruction of a plane cut through a body

Consider a finite body that is exposed to impinging collimated light, cf. Fig. 2. The interaction between the body and the light is assumed to be restricted to

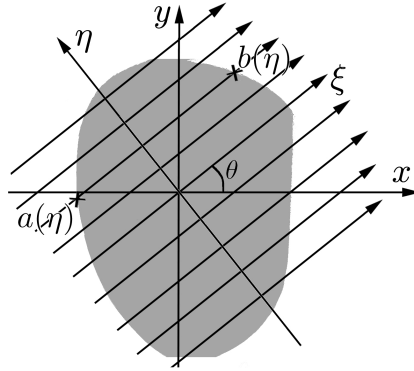


Figure 2: Light impinging on a semitransparent body. The  $a(\eta)$  and  $b(\eta)$  mark the entrance and exit of the x-ray.

attenuation of the light only, while it stays collimated. Two cartesian coordinate systems  $x$ - $y$  and  $\xi$ - $\eta$  with common origin are attached to a plane cross-section of the body. The  $\xi$  axis is rotated the angle  $\theta$  from the  $x$ -axis as is shown in Fig. 2. A polar coordinate system is defined as  $\rho = \sqrt{x^2 + y^2}$  and  $\theta = \arctan(y/x)$ .

Consider a single beam of light that transverses the body in the positive  $\xi$ -direction, i.e., at a constant  $\eta$ . Along its path the light intensity  $I = I(\xi, \eta)$  becomes attenuated at a rate  $dI/d\xi$ . The optical density  $\mu$  of the material causes the attenuation and is supposed to vary in the plane. The attenuation rate is also assumed to be proportional to the intensity  $I$  and therefore,

$$dI(\xi, \eta)/d\xi = -\mu(\xi, \eta)I(\xi, \eta). \quad (1)$$

Integration readily gives the optical density as,

$$\mu(\xi, \eta) = -\frac{d}{d\xi} \ln I(\xi, \eta). \quad (2)$$

The light crosses the body boundary twice, i.e., at entrance  $\xi_a = a(\eta)$  and when it leaves the body at  $b(\eta)$ , see Fig. 2. Integration is performed along the  $\xi$ -axis from the entry, where the impinging intensity,  $I_o$ , is assumed to be independent of  $\eta$ . After the exit of the body at  $\xi_b = b(\eta)$  the intensity remains independent of  $\xi$ , i.e., from (2) we get

$$I(\xi, \eta)/I_o = \exp\left[\int_a^\xi \mu(\xi', \eta)d\xi'\right] = \begin{cases} 1 & \text{for } \xi \leq a(\eta) \\ \exp\left[\int_a^\xi \mu(\xi', \eta)d\xi'\right] & \text{for } a(\eta) < \xi < b(\eta) \\ \exp\left[\int_a^b \mu(\xi', \eta)d\xi'\right] & \text{for } \xi \geq b(\eta) \end{cases}. \quad (3)$$

The light intensity  $I(\eta)$  remaining after passing the body at  $\xi = b$  is given by

$$\ln[I(\eta)/I_o] = f(b, \eta) - f(a, \eta), \quad \text{where} \quad f(\eta) = \int_a^b \mu(\xi, \eta) d\xi, \quad (4)$$

Consider now, multiple exposures as described above but now from different angles. For the full exposure of the body let the function  $g = g(\rho, \theta)$  be defined as follows

$$g(\rho, \theta) = \int_A \mu(x, y) \delta(x \cos \theta + y \sin \theta - \rho) dx dy, \quad (5)$$

where  $\delta$  is Dirac's delta function. Assume further that  $\mu(x, y)$  is unknown and that  $g(\rho, \theta)$  is a known function. The Radon inverse transformation is closely related to the inverse Fourier transform and is given by [10, 11] as

$$\mu(x, y) = \frac{1}{2\pi^2} \int_{-\infty}^{\infty} \int_0^{\pi} \frac{\partial g(\rho, \theta)}{\partial \rho} \frac{d\rho d\theta}{x \cos \theta + y \sin \theta - \rho}. \quad (6)$$

With the known projection  $g(\rho, \theta)$  the solution is readily given through numerical integration of (6). With the irregular geometry of the bone cross-section one cannot hope for an analytical solution. However, the close connection to the Fourier transform with a developed formalism for obtaining discretising solutions for both the transform and its corresponding inverse transform, can be utilised as is described in the following section.

#### 4. Numerical analysis

The numerical approximation of the optical density  $\mu(x, y)$  relies on the accuracy and resolution of the measured intensity function  $g(\rho, \theta)$ . By discretising on the pixel level, a resulting accurate density  $\mu(x, y)$  is anticipated. The discretised integral approximating (6) may be written

$$\mu(x, y) = \{\mathfrak{R}^{-1}g\}(x, y). \quad (7)$$

by organising the discrete pixel intensities representing the functions  $\mu(x, y)$  and  $g(\rho, \theta)$  in vectors  $\boldsymbol{\mu}$  and  $\boldsymbol{g}$ . We may write (7) as a system of equations

$$\boldsymbol{\mu} = \boldsymbol{A}\boldsymbol{g} \quad (8)$$

where  $\boldsymbol{\mu}$  and  $\boldsymbol{g}$  have the dimension  $N$  and hence  $\boldsymbol{A}$  is an  $N \times N$  matrix. The basic images  $\{h_j(x, y)\}_{j=1}^J$  are defined by

$$h_j(x, y) = \begin{cases} 1 & \text{if } (x, y) \in \text{pixel no. } j \\ 0 & \text{otherwise} \end{cases}, \quad (9)$$

and the image is written

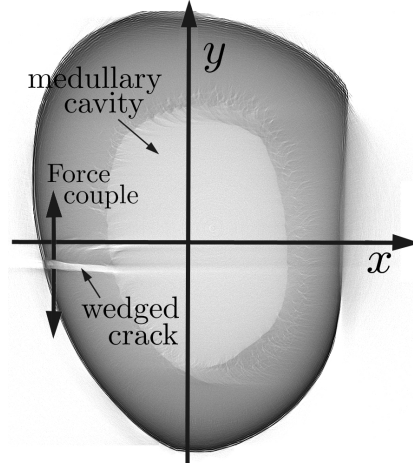


Figure 3: The obtained density field of the selected cross-section. The studied densities are at  $x = 0$  and at  $y = 0$ . The crack is the white cut vaguely visual near the negative  $x$ -axis. The contrasting density that vanishes in the empty opened crack creates an optical ghost mark that is seen stretching into the medullary cavity.

$$g(x, y) = \sum_{j=1}^J c_j h_j(x, y), \quad (10)$$

where  $J$  is the number of pixels. The coefficients  $c_j$  can be determined provided that the number of projections is equal or larger than the number of pixels,  $J$ . A more detailed description of the numerics that come with the discrete inverse Radon Transform is given in [10].

## 5. Results and discussion

In the present study a total of 20 planes below and above a selected cross-section as shown in Fig. 2b) are averaged and used for the reconstruction of the optical density  $\mu(x, y)$  represented as a 2D image.

Cartesian coordinates  $x$  and  $y$  are chosen along the shorter,  $x$ , respectively the longer,  $y$ , axes of the ellipsoidal cross-section (cf. Fig. 3). The initial incident x-rays are parallel with the  $x$ -axis. The approach is to rotate the specimen 360 degrees around an axis perpendicular to the  $x$ - $y$  plane. During a couple of minutes 6284 scans are made.

Each scan gives a line of intensities such as the marked line in the image taken at the first scan, i.e. Fig. 2. All 6284 give a 1D view of the selected plane from different angles 0 to 360 degrees. Together these define the function  $g(x, y)$ . The optical density  $\mu(x, y)$  is then obtained from (6), utilising the numerical scheme described in Sect. 4. The numerical solution of (8) is obtained by using the software Mathematica v.8. [12]

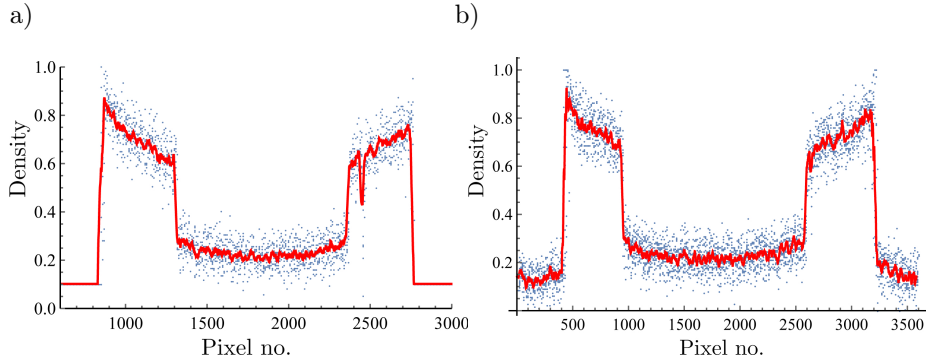


Figure 4: Bone densities along a) the  $x$ -axis ( $y=0$ ), b) the  $y$ -axis ( $x=0$ ), cf. Fig. 3. The blue dots are the actual optical densities  $\mu(x, y)$  and the red curves are the filtered dittos.

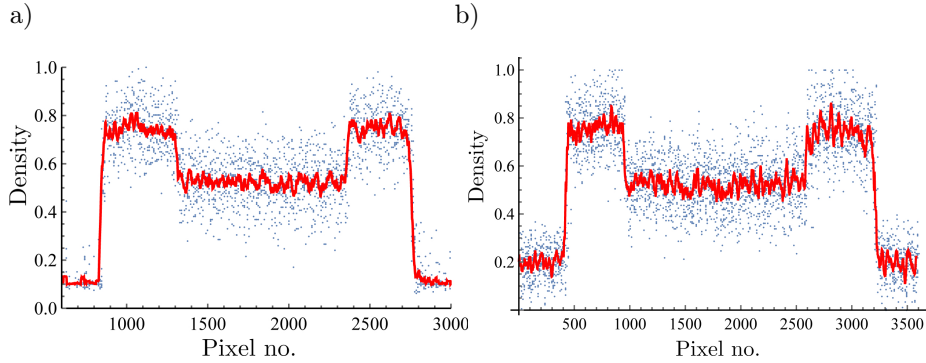


Figure 5: Bone and iodine inserted in the medullary cavity. Densities obtained along a) the  $x$ -axis, b) the  $y$ -axis. The pure iodine is inserted in the medullary cavity between pixels 1000-2600 along the  $x$ -axis and 1300-2800 along the  $y$ -axis.

Figure 4 shows the original optical density for the bone, along a)  $x = 0$  and b)  $y = 0$ , i.e.  $\mu(0, y)$  and  $\mu(x, 0)$  respectively. The vague swarm of blue marks is the obtained data which suffers from a large scatter with a range of around  $\pm 20\%$ . The data is filtered as a moving average obtained at each current pixel as the average of the 10 previous and 10 coming pixels.

As observed the bone density in both directions has an expected increase of the density towards the periosteal surface. A small but false density is observed in the area covered by the medullary cavity that is empty. If this is an optical effect that originates from the scanned images or occurs as a consequence of insufficient numerical accuracy, is at present not known.

In the next step iodine was inserted into the medullary cavity that was filled only to around 60% of its volume to avoid contamination of the upper part of the sample. Apart from the present iodine the procedure from the first sequence is followed. After 20 minutes a second series of images was captured. Fig. 5 shows the results. The striking difference is that the density inside the medullary

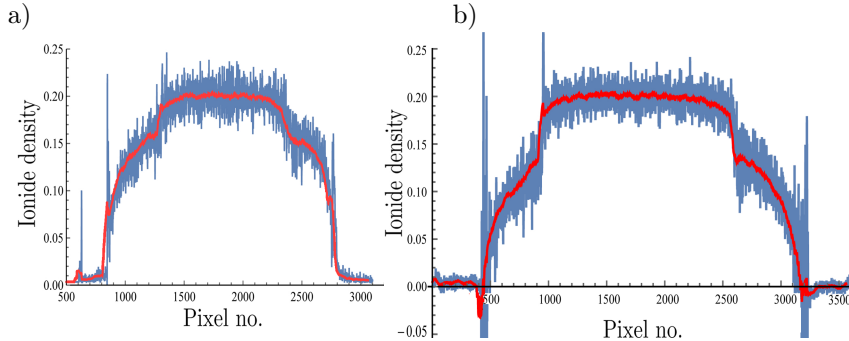


Figure 6: The change of the optical density caused by the iodine for projections along a) the  $x$ -axis, b) the  $y$ -axis.

cavity has increased to more than 70% of that in the bone. Also the less dense inner parts of the bone display an increased density and reaches that of the previously obtained density for the bone areas closest to the periosteal surface. Visually the scatter, i.e. the blue raw data dots, is larger and closer to around  $\pm 30\%$ .

By taking the difference between the raw data without and with the iodine, the distribution of the iodine is obtained. The result that is displayed in Fig. 6 clearly shows how the iodine has penetrated into the bone. The concentration decreases and drops to practically zero at the periosteal surface. The distributions along  $x = 0$  and  $y = 0$  both have the same characteristics, with the medullary cavity having a fairly constant density and with a rapid drop at the inner bone surface. In the bone the iodine density decreases and almost vanishes close to the periosteal surface. This decrease may be caused by the known increase of the bone density, leaving less space impeding the mobility of the iodine.

Along the  $x$ -axis, cf. Fig. 6a), the iodine concentration decays more rapidly in the bone section at  $x < 0$  where the load is compressive and small as compared with the bone section at  $x > 0$ , where the iodine concentration is almost constant to around a third of the section. Closer to the periosteal surface the concentration drops rapidly. A preliminary explanation is that the section at  $x > 0$  is the large bending stresses. These give a large tensile stress on the medullary cavity side and compression on the periosteal side.

Along the  $y$ -axis, cf. Fig. 6b), the iodine concentrations in both bone sections  $y < 0$  and  $y > 0$  are fairly similar. Further the distributions of the iodine are close to what is observed in the bone section with small load, i.e., at  $x < 0$  and  $y = 0$ . A possible reason is that these sections have a combination of rather thick cross sections and are exposed to only half of the bending stresses that are present in the section at  $x > 0$ ,  $y = 0$ .

## 6. Conclusions

An x-ray scan of a short section of a bovine long bone was performed. The specimen was exposed to mechanical stress via wedge forced into a longitudinal crack. Scans were performed with and without iodine inserted into the medullary cavity. 6284 scanned images were taken during rotation of the specimen.

Two cross-section images before respectively after the exposure to iodine are computed using Radon's inverse transform. The iodine penetration into the bone was obtained as the differences between the two cross-section images.

In conclusion the preliminary result is that the part of the cross-section having the largest stress gradient has absorbed the highest amount of iodine. Hence the study strengthens the hypotheses about stress-driven diffusion in bone tissue suggested in [4, 5].

## Acknowledgment

The authors would like to thank The Royal Institute of Technology for supporting G. Lindberg during a two year postdoc position. Prof. Philip Withers, is acknowledged for allowing us to perform the experiments at The Henry Moseley X-ray Imaging Facility, Photon Science Institute at the University of Manchester and Prof. C. Bjerkén at Malmö University is acknowledged for assisting at the preparation of bone samples and during the scanning.

## References

- [1] L. Xie, J.M. Jacobson, E.S. Choi, B. Busa, L.R. Donahue, L.M. Miller, C.T. Rubin, S. Judex, Low-level mechanical vibrations can influence bone resorption and bone formation in the growing skeleton, *Bone* 39 (2006) 1059.
- [2] T.S. Gross, J.L. Edwards, K.J. McLeod, C.T. Rubin, Strain gradients correlate with sites of periosteal bone formation, *J. Bone Miner. Res.* 12 (1997) 982.
- [3] M. Isaksson, C.C. van Donkelaar, R. Huiskes, K. Ito, Corroboration of mechanoregulatory algorithms for tissue differentiation during fracture healing: comparison with in vivo results, *J. Orthop. Res.* 24 (2006) 898.
- [4] G. Lindberg, L. Banks-Sills, P. Ståhle, I. Svensson, A two-dimensional model for stress driven diffusion in bone tissue, *Comput. Methods Biomech. Biomed.Eng.* 19 (5) (2015) 457, <https://doi.org/10.1080/10255842.2013.807507>.
- [5] G. Lindberg, P. Ståhle, Growth of a long bone cross section - A 2D phase-field model, *Math. Biosciences* 313 (2019) 1.



- [6] L. Banks-Sills, P. Stähle, I. Svensson, E. Eliaz, Strain driven transport for bone modeling at the periosteal surface, *Math. Biosciences* 230 (2011) 37.
- [7] L.E. Lanyon, C.T. Rubin, Static vs dynamic loads as an influence on bone remodelling, *J. Biomech.* 17 (1984) 897.
- [8] A. Einstein [diffusion 1905] [28] A. Einstein, The motion of elements suspended in static liquids as claimed in the molecular kinetic theory of heat, *Ann. Phys. Leipzig* 17 (1905) 549.
- [9] M. v. Smoluchowski, Theory accompanied by a general discussion of fluctuations is given by A. Einstein, *Ann. d. Physik* 4, (1909) 25.
- [10] B. Gustafsson, Mathematics for Computer Tomography, *Physica Scripta*. T61 (1996) 38.
- [11] L. Radon, "Über die Bestimmung von Funktionen durch ihre Integralwerte langs gewisser Mannigfaltigkeiten", *Ber. Verh. Sachs. Akad. der Wissensch., Math.-Phys.* 69 (1917) 262.
- [12] S. Wolfram, "The Mathematica Book", Ed. 5, Wolfram Media Inc., 1488pp, ISBN:1579550223, *Mathematica v. 8* (2003)